AIP Advances

Defect, transport, and dopant properties of andradite garnet $Ca_3Fe_2Si_3O_{12}$

Cite as: AIP Advances **10**, 075004 (2020); https://doi.org/10.1063/5.0012594
Submitted: 04 May 2020 • Accepted: 15 June 2020 • Published Online: 01 July 2020

Navaratnarajah Kuganathan, Sashikesh Ganeshalingam and Alexander Chroneos

Defect, transport, and dopant properties of andradite garnet $Ca_3Fe_2Si_3O_{12}$

Cite as: AIP Advances 10, 075004 (2020); doi: 10.1063/5.0012594
Submitted: 4 May 2020 • Accepted: 15 June 2020 •
Published Online: 1 July 2020

Navaratnarajah Kuganathan,[1,2,a] Sashikesh Ganeshalingam,[3] and Alexander Chroneos[1,2]

AFFILIATIONS

[1] Department of Materials, Imperial College London, London SW7 2AZ, United Kingdom
[2] Faculty of Engineering, Environment and Computing, Coventry University, Priory Street, Coventry CV1 5FB, United Kingdom
[3] Department of Chemistry, University of Jaffna, Sir. Pon Ramanathan Road, Thirunelvely, Jaffna 40000, Sri Lanka

[a] **Author to whom correspondence should be addressed:** n.kuganathan@imperial.ac.uk and ad0636@coventry.ac.uk

ABSTRACT

There is growing interest to discover suitable calcium containing oxides that can be used as electrode materials in calcium ion batteries. A comprehensive computational investigation of ionic defects and Ca-ion diffusion in Ca-bearing oxide materials at the atomic level is important so as to predict their suitability for use in Ca-ion batteries. In this study, we apply atomistic simulation techniques to examine the energetics of defects, dopants, and Ca-ion diffusion in $Ca_3Fe_2Si_3O_{12}$. The calculations suggest that the Ca/Fe anti-site defect is the most favorable intrinsic defect causing such significant disorder, which would be sensitive to synthesis conditions. Diffusion of Ca^{2+} ions within $Ca_3Fe_2Si_3O_{12}$ is three-dimensional, with the activation energy of migration of 2.63 eV inferring slow ionic conductivity. The most favorable isovalent defects are Mn^{2+}, Sc^{3+}, and Ge^{4+} on Ca, Fe, and Si, respectively, for this process. The formation of extra calcium was considered to increase the capacity and diffusion of Ca in this material. It is found that Al^{3+} and Mn^{2+} are the candidate dopants on the Si and Fe sites, respectively, for this process and there is a reduction observed in the activation energies. The electronic structures of favorable dopant configurations are discussed using density functional theory simulations.

I. INTRODUCTION

Although lithium-ion batteries have dominated for years,[1–4] calcium-ion batteries (CIBs) are gaining attraction for large-scale storage applications due to cost, abundance, and enhanced safety.[5,6] Compared to other multivalent battery systems such as Mg-ion batteries,[7,8] the research activity of CIBs is in the early stage. CIBs are also expected to provide high energy and power density due to their two-electron reaction during intercalation. Furthermore, the electrode potential of Ca/Ca^{2+} is lower by 0.5 eV than that of Mg/Mg^{2+} and higher only by 0.1 eV than that of Li/Li^{+}, implying higher cell voltage.[9]

Identification of suitable electrode materials is important in the development of CIBs. There are only a few published studies on electrode materials including layered compounds (e.g., V_2O_5),[10] chevrel phases [e.g., $CaMo_6X_8$ (X = S, Se, and Te)],[11] and Prussian blue analogs [e.g., $NaMnFe(CN)_6$][9] for CIBs. Arroyo-de Dompablo *et al.*[12] recently carried out a joint experimental and theoretical study on $CaMn_2O_4$ polymorphs and concluded that full Ca extraction from these polymorphs introduces a substantial volume change with an average voltage of 3.1 V and a high Ca-ion migration barrier. In a recent theoretical study, Torres *et al.*[13] considered a few Ca based minerals including $Ca_3Mn_2(SiO_4)_3$, $CaMn(SiO_3)_2$, and $CaMn(CO_3)_2$ to calculate their diffusion barriers, average voltages, and volume changes over Ca de-insertion.

Materials consisting of iron with structures formed by linking through polyhedral units such as PO_4, SiO_4, and SO_4, to provide structural stability, are of considerable interest in the development of electrode materials.[14–16] Andradite ($Ca_3Fe_2Si_3O_{12}$)[17] is a rock-forming silicate garnet and consists of three Ca^{2+} ions per formula unit, leading to high theoretical capacity, and SiO_4^{4-} units offering structural stability via strong Si–O bonds. Furthermore, the low cost and availability of iron and silicon coupled with their non-toxicity also make this material ideal.

Computer modeling techniques based on pair-wise potentials are powerful tools to predict and understand the defects, ion transport, and dopant properties in solid-state oxide materials. A variety of oxide materials including battery materials have been examined using this technique.[18–22] In the present study, using inter-atomic pair potentials, we characterize the defect, diffusion, and dopant properties of $Ca_3Fe_2Si_3O_{12}$ on an atomistic level. Furthermore, density functional theory (DFT) allowed us to study the electronic structures of doped configurations.

II. COMPUTATIONAL METHODS

Defect, diffusion, and dopant calculations were performed using the classical pair potential method as implemented in the GULP code,[23] which describes ionic interactions in the form of long-range Coulomb attractions and short-range attractions (electron–electron repulsion and attractive dispersion). Buckingham potentials (refer to Table S1) were used to describe short-range interactions. Cell parameters and ionic positions were relaxed using the Broyden–Fletcher–Goldfarb–Shanno (BFGS) algorithm.[24] Defects were modeled using the Mott–Littleton method.[25] Ca-ion migration was calculated by considering two adjacent Ca vacancy sites as initial and final configurations. Seven interstitial Ca ions were considered in a direct linear route, and they were allowed to relax. The difference between the vacancy formation energy and the maximum energy along the diffusion path is defined as the activation energy of migration. Relative energies and trends will be consistent although the present model assumes that ions are fully charged and defect concentrations are at a dilute limit. Thermodynamically, the defect parameters (i.e., migration energies) can be defined through the comparison of the defective crystal to an isobaric (or isochoric) non-defective crystal. These defect formation parameters are interlinked by thermodynamic relations.[26,27] The present calculations correspond to the isobaric parameters for the formation and the migration processes.[28,29]

Electronic structure calculations are based on DFT using plane wave basis sets and projected augmented wave (PAW) potentials. A plane wave DFT code VASP (Vienna *Ab initio* Simulation Package)[30] which diagonalizes the Kohn–Sham equations was used. The calculations were performed using the generalized gradient approximation (GGA) as proposed by Perdew, Burke, and Ernzerhof (PBE).[31] In all cases, a plane wave basis set with a cut-off of 500 eV and a 2 × 2 × 2 Monkhorst and Pack[32] k-point mesh were used. Energy minimization calculations were performed using the conjugate gradient (CG) algorithm[33] and a force tolerance value of 0.001 eV/Å. Short-range attractive interactions (dispersion) were modeled using a DFT + D3 method as implemented by Grimme *et al.*[34]

III. RESULTS AND DISCUSSION

A. Crystal structure of $Ca_3Fe_2Si_3O_{12}$

The crystal structure of $Ca_3Fe_2Si_3O_{12}$ at room temperature is cubic (space group $Ia\bar{3}d$, no. 230).[17] Experimental lattice parameters reported by Novak and Gibbs.[17] are a = b = c = 12.058 Å, α = β = γ = 90°, and V = 1753.18 Å^3. An eight-fold coordination is observed for Ca^{2+} cations. The Fe^{2+} ions reside in the FeO_6 octahedra. Tetrahedral (SiO_4) units share their corners with FeO_6 units in a three-dimensional network, as shown in Fig. 1. Energy minimization calculation was performed to relax both ionic positions and cell dimensions in order to obtain equilibrium lattice parameters. The results allowed us to check the quality of the Buckingham potentials used in the classical simulation and pseudopotentials together with basis sets used in the DFT simulation. There is good agreement between calculated and experimental values (refer to Table I).

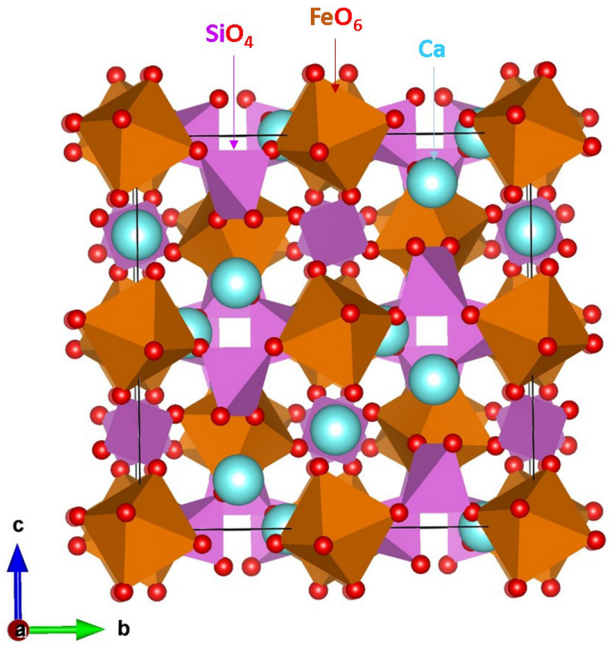

FIG. 1. Crystal structure of $Ca_3Fe_2Si_3O_{12}$.[17]

B. Intrinsic atomic defects

Diffusion of ions in an ionic material is typically influenced by Schottky and Frenkel disorders, which can be calculated by combining point defects (vacancies and interstitials). These point defect

TABLE I. Calculated and experimental parameters of $Ca_3Fe_2Si_3O_{12}$.

	Calculated			|Δ| (%)	
Parameter	Force field	DFT	Experiment[17]	Force field	DFT
a (Å)		12.061			0.02
b (Å)	12.090	12.064	12.058	0.27	0.05
c (Å)		12.066			0.07
α (deg)		90.21			0.23
β (deg)	90.00	90.05	90.00	0.00	0.06
γ (deg)		89.96			0.04
V (Å^3)	1767.20	1755.55	1753.18	0.80	0.14

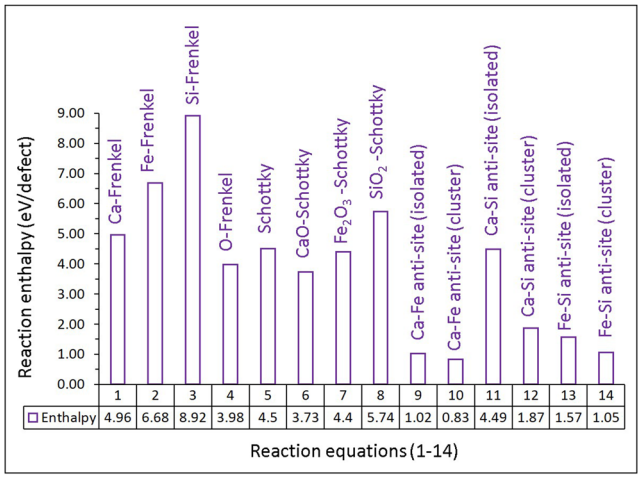

FIG. 2. Reaction enthalpies calculated for different defect processes.

energies can be difficult to determine via experimentation. The current classical simulation technique allowed us to calculate a series of point defects. The lowest energy point defects were then combined to calculate Frenkel and Schottky defect processes. Anti-site defects in which cations exchange their positions were also calculated as these defects have been observed in many oxide materials both experimentally and theoretically.[35–40] Here, we write reaction equations for all possible Schottky, Frenkel, and anti-site defects in $Ca_3Fe_2Si_3O_{12}$ using the Kröger–Vink notation,[41]

$$\text{Ca Frenkel} : Ca_{Ca}^{X} \rightarrow V_{Ca}'' + Ca_i^{\cdot\cdot}, \quad (1)$$

$$\text{Fe Frenkel} : Fe_{Fe}^{X} \rightarrow V_{Fe}''' + Fe_i^{\cdot\cdot\cdot}, \quad (2)$$

$$\text{Si Frenkel} : Si_{Si}^{X} \rightarrow V_{Si}'''' + Si_i^{\cdot\cdot\cdot\cdot}, \quad (3)$$

$$\text{O Frenkel} : O_O^{X} \rightarrow V_O^{\cdot\cdot} + O_i'', \quad (4)$$

$$\text{Schottky} : 3Ca_{Ca}^{X} + 2Fe_{Fe}^{X} + 3Si_{Si}^{X} + 12O_O^{X} \rightarrow 3V''_{Ca} + 2V'''_{Fe} + 3V_{Si}'''' + 12V_O^{\cdot\cdot} + Ca_3Fe_2Si_3O_{12}, \quad (5)$$

$$\text{CaO Schottky} : Ca_{Ca}^{X} + O_O^{X} \rightarrow V_{Ca}'' + V_O^{\cdot\cdot} + CaO, \quad (6)$$

$$Fe_2O_3\ \text{Schottky} : 2Fe_{Fe}^{X} + 3O_O^{X} \rightarrow 2V_{Fe}'' + 3V_O^{\cdot\cdot} + Fe_2O_3, \quad (7)$$

$$SiO_2\ \text{Schottky} : Si_{Si}^{X} + 2O_O^{X} \rightarrow V_{Si}'''' + 2V_O^{\cdot\cdot} + SiO_2, \quad (8)$$

$$\text{Ca/Fe antisite (isolated)} : Ca_{Ca}^{X} + Fe_{Fe}^{X} \rightarrow Ca_{Ca}' + Fe_{Ca}^{\cdot}, \quad (9)$$

$$\text{Ca/Fe antisite (cluster)} : Ca_{Ca}^{X} + Fe_{Fe}^{X} \rightarrow \left\{Ca_{Fe}' : Fe_{Ca}^{\cdot}\right\}^{X}, \quad (10)$$

$$\text{Ca/Si antisite (isolated)} : Ca_{Ca}^{X} + Si_{Si}^{X} \rightarrow Ca_{Si}'' + Si_{Ca}^{\cdot\cdot}, \quad (11)$$

$$\text{Ca/Si antisite (cluster)} : Ca_{Ca}^{X} + Si_{Si}^{X} \rightarrow \left\{Ca_{Si}'' : Si_{Ca}^{\cdot\cdot}\right\}^{X}, \quad (12)$$

$$\text{Fe/Si antisite (isolated)} : Fe_{Fe}^{X} + Si_{Si}^{X} \rightarrow Fe_{Si}' + Si_{Fe}^{\cdot}, \quad (13)$$

$$\text{Fe/Si antisite (cluster)} : Fe_{Fe}^{X} + Si_{Si}^{X} \rightarrow \left\{Fe_{Si}' : Si_{Fe}^{\cdot}\right\}^{X}. \quad (14)$$

Figure 2 shows the resulting defect energies. The most favorable intrinsic disorder type is the Ca–Fe anti-site defect cluster (0.83 eV/defect). In this defect process, it is anticipated that there would be some Ca^{2+} ions on the Fe site and Fe^{3+} ions on the Ca site. In the isolated form of the anti-site defect, defects were modeled individually, and their energies were combined. Both defects were considered simultaneously in the cluster form. The energy difference between the isolated and cluster forms is considered as the binding energy (−0.19 eV). Notably, other anti-site defect cluster energies (Ca–Si and Fe–Si) are lower than the Schottky and Frenkel defect energies. Among other defect processes, the CaO Schottky is the lowest energy process, with a defect energy of 3.73 eV/defect. This process will facilitate the formation of V_{Ca}'' and $V_O^{\cdot\cdot}$ at high temperatures. The oxygen Frenkel energy is calculated to be 3.98 eV/defect, with a deviation of only 0.25 eV from the CaO Schottky. However, the Ca Frenkel energy is calculated to be ~5.00 eV, inferring that the formation of Ca vacancies is not significant. Other Frenkel and Schottky energies are highly endoergic, suggesting that they will not be present at significant concentrations.

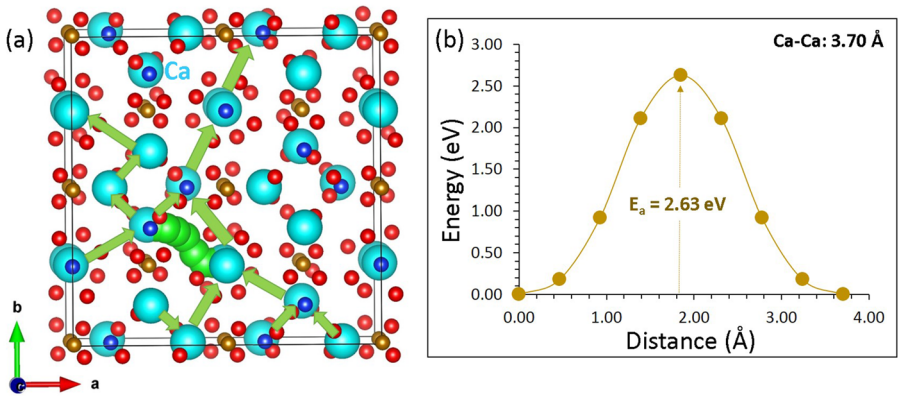

FIG. 3. (a) Long range Ca-ion diffusion pathways and (b) the energy profile diagram showing the activation energy.

C. Self-diffusion of Ca^{2+} ions

The diffusion of Ca^{2+} ions is discussed in this section. A material with high ionic conductivity generally exhibits a high rate performance and is suitable as an electrode for use in devices such as batteries. Classical simulation allowed us to calculate the Ca-ion diffusion pathways and the corresponding activation energies in $Ca_3Fe_2Si_3O_{12}$. In general, diffusion pathways are difficult to examine in the experiment, particularly for complex oxides such as $Ca_3Fe_2Si_3O_{12}$. The current classical simulation technique has been successfully applied in previous studies to calculate ion migration pathways together with activation energies.[42,43] For example, the Li-ion migration pathway calculated in $LiFePO_4$ by Fisher *et al.*[44] was in excellent agreement with the neutron diffraction experiment.[45]

A potential Ca–Ca hop with a jump distance of 3.70 Å was identified. Many of these identical hops were then connected to form a three-dimensional long-range migration path, as shown in Fig. 3. The activation energy for this hop is calculated to be 2.63 eV, and Ca-ions migrate in a curved pathway. High activation energy of Ca^{2+} ion migration in $Ca_3Fe_2Si_3O_{12}$ shows that the Ca-ion diffusion is slow in this material. A possible solution to increase the ion diffusion is by reducing the Ca–Ca distance in this material via synthesizing nanoparticles.[46] Table II lists the activation energies calculated for Ca-ion migration in different Ca-based oxide materials.[12,13,47] Torres *et al.*[13] recently performed DFT calculations on a variety of Ca based minerals and reported the activation energies of Ca-ion migration. Interestingly, $Ca_3Cr_2Si_3O_{12}$ and $Ca_3Mn_2Si_3O_{12}$ materials, isostructural with $Ca_3Fe_2Si_3O_{12}$, were also considered, and their activation energies of migration were reported to be 2.07 eV and 2.09 eV, respectively.[13] Activation energies calculated for Ca-ion migration are lower by ~0.50 eV than those calculated in a similar $Ca_3Fe_2Si_3O_{12}$ structure. This is due to different methodologies considered and different transition elements present in the crystal structures. Activation energies are greater than 2 eV in all cases, inferring poor ionic conductivity. A possible reason can be due to the strong electrostatic interaction between the migrating Ca^{2+} cations and the other ions in the lattice.

D. Solution of dopants

This section examines the introduction of cations via divalent, trivalent, and tetravalent doping into $Ca_3Fe_2Si_3O_{12}$. Doping can result in beneficial or detrimental effects on the material. In particular, suitable dopants can stabilize a material in order to prevent unfavorable phase transformations. The aim here is to provide guidance to the dopants that require the least energy to integrate into the lattice, the effects of which can be studied in subsequent experimental testing.

TABLE II. Activation energies calculated for Ca-ion migration in Ca containing materials.

Ca-based oxide material	Activation energy (eV)
$CaFeSi_2O_6$	4.36[47]
$Ca_3Mn_2Si_3O_{12}$	2.09[13]
$CaMnSi_2O_6$	4.60[13]
$Ca_3Cr_2Si_3O_{12}$	2.07[13]
$Ca_{11}Mn_{12}C_{24}O_{72}$	2.80[13]
$CaMn_2O_4$	1.00[12]

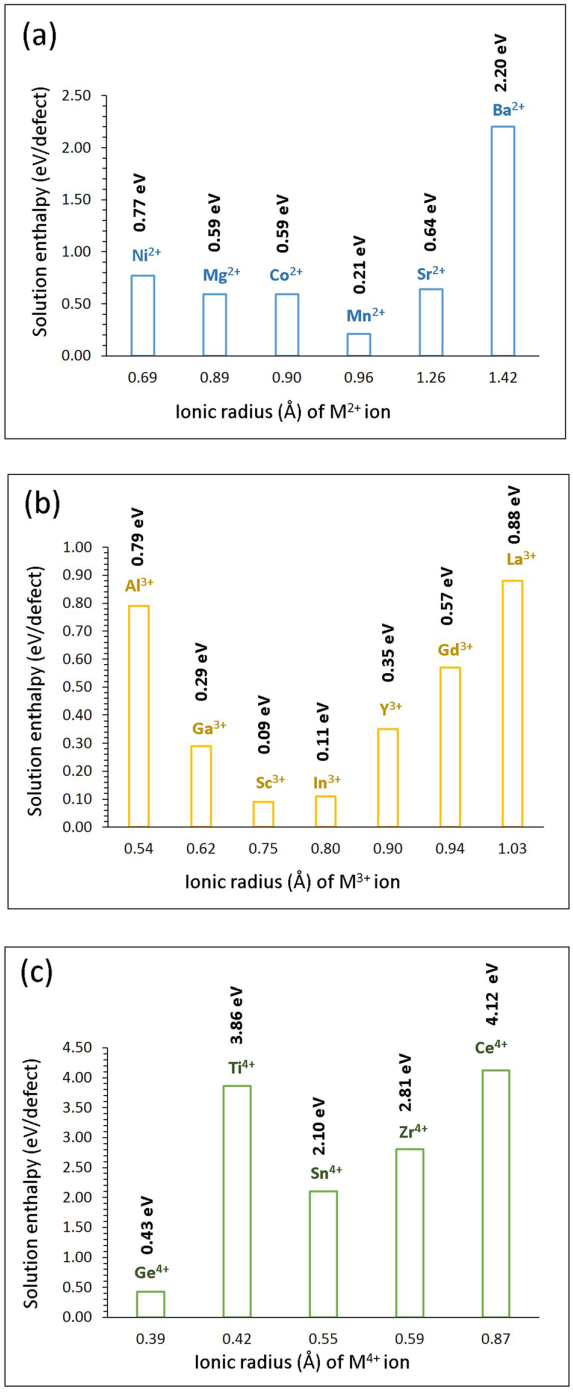

FIG. 4. Solution enthalpies calculated for (a) divalent, (b) trivalent, and (c) tetravalent dopants on the Ca, Fe, and Si sites, respectively.

1. Divalent dopants

Divalent cations (M = Ni, Mg, Co, Mn, Sr, and Ba) were first considered for doping on the Ca site. The doping mechanism can be seen in the following equation:

$$MO + Ca_{Ca}^{X} \rightarrow M_{Ca}^{X} + CaO. \quad (15)$$

The calculated solution enthalpies are reported in Fig. 4. The lowest solution enthalpy (0.21 eV) is predicted for Mn^{2+}, inferring the highest solubility. The lowest solution enthalpy suggests that Mn^{2+} would be an ideal candidate to stabilize $Ca_3Fe_2Si_3O_{12}$. The ionic radius of Ca^{2+} in an eight coordination environment is 1.00 Å. Favorability of the Mn^{2+} dopant can be due to its ionic radius (0.96 Å), which is close to the ionic radius of the Ca^{2+} ion. Both Mg^{2+} and Co^{2+} exhibit an identical solution enthalpy of 0.59 eV. This is due to a very small difference in their ionic radii. Solution enthalpy increases with the difference in the ionic radius between dopants and the Ca^{2+} ion. The solution enthalpies of Sr^{2+} and Ni^{2+} were calculated to be 0.64 eV and 0.77 eV, respectively. The highest solution enthalpy of 2.20 eV is calculated for Ba^{2+}, suggesting that this dopant is very unfavorable for doping on the Ca site.

To increase the capacity of $Ca_3Fe_2Si_3O_{12}$, divalent dopants were considered on the Fe site. The following reaction equation [Eq. (16)] shows that this doping strategy can introduce additional Ca^{2+} ions in the form of Ca interstitials in the lattice. A previous experimental study considered Co^{3+} doping on the Ru site in Li_2RuO_3 to increase the Li^+ concentration, and doping resulted in an enhancement in the electrochemical reversibility of Li^+ ions and the concentration of Li^+ ions in the lattice,[48]

$$2MO + 2Fe_{Fe}^{X} + CaO \rightarrow 2M'_{Fe} + Ca_i^{\cdot\cdot} + Fe_2O_3. \quad (16)$$

The favorable dopant for this process is Mn^{2+}, and its solution energy is calculated to be 3.36 eV. Solution energies calculated for Co^{2+}, Ni^{2+}, Mg^{2+}, and Zn^{2+} are very close to the value calculated for Mn^{2+}; therefore, they are also candidate dopants for experimental testing (refer to Fig. 5). The ionic radius of Fe^{3+} is 0.65 Å. Favorability of the five dopants (Mn, Co, Ni, Mg, and Zn) is due to their ionic radii (0.65 Å–0.74 Å) matching closely with the ionic radius of Fe^{3+}. The ionic radius of Sr^{2+} (1.18 Å) deviates significantly from that of Fe^{3+}, reflecting in solution enthalpy. The highest positive solution enthalpy of 6.17 eV is calculated for Ba^{2+}, suggesting that this dopant is highly unfavorable on the Fe site.

2. Trivalent dopants

Here, we consider a range of trivalent cations (M = Al, Ga, In, Sc, Y, Gd, and La) on the Fe and Si sites. Doping on the Fe site produced no charge compensating defects as the charge on Fe is +3 [refer to Eq. (17)]. Solution enthalpies are plotted as a function of ionic radii of dopants in Fig. 4(b),

$$M_2O_3 + 2Fe_{Fe}^{X} \rightarrow 2M_{Fe}^{X} + Fe_2O_3. \quad (17)$$

The most favorable dopant is Sc^{3+}, with a solution enthalpy of 0.09 eV. The solution enthalpy of In^{3+} is higher only by 0.02 eV than that calculated for Sc^{3+}, meaning that In^{3+} is also a promising dopant. Favorability of these two dopants can be partly due to their ionic radii being closer to the ionic radius of Fe^{3+} (0.65 Å). The solution enthalpy of Ga^{3+} is 0.29 eV although its ionic radius (0.62 Å) is very close to the ionic radius of Fe^{3+}. Other dopants exhibit high solution enthalpies due to their ionic radii deviating from the ionic radius of Fe^{3+} [refer to Fig. 4(b)].

The formation of additional Ca^{2+} ions in the lattice was considered by doping trivalent cations on the Si site. As we discussed earlier, this process can also introduce Ca interstitials, as shown in the following reaction,

$$M_2O_3 + 2Si_{Si}^{X} + CaO \rightarrow 2M'_{Si} + Ca_i^{\cdot\cdot} + 2SiO_2. \quad (18)$$

The solution enthalpies are reported in Fig. 5(b). In all cases, solution enthalpies are highly positive (>5 eV), suggesting that this process required high energy possibly in the form of heat. The most favorable dopant is Al^{3+}, with a solution enthalpy of 5.49 eV. The lowest solution enthalpy for Al^{3+} can be due to its ionic radius (0.39 Å) being closer to the ionic radius of Si^{4+} (0.26 Å). High endoergic solution enthalpy for this mechanism can be due to the high defect formation energy of quadruply charged Si.

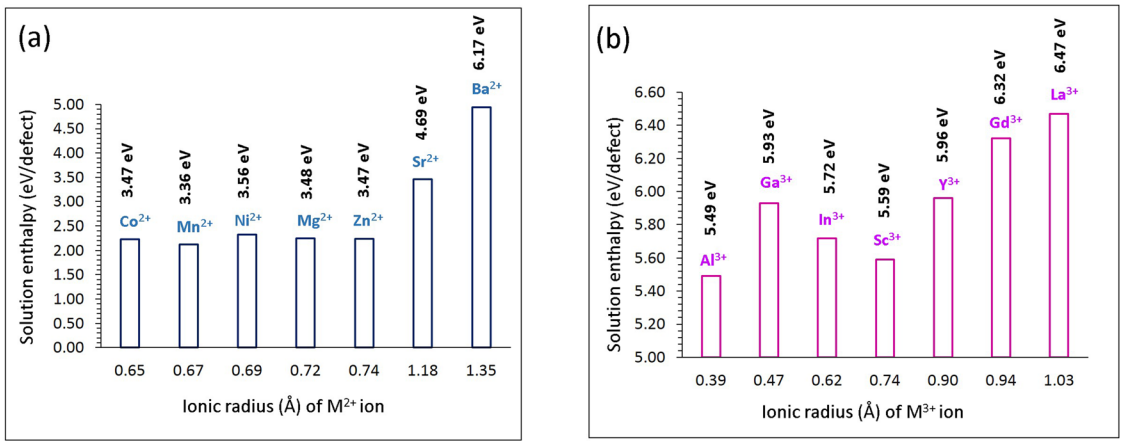

FIG. 5. Solution enthalpies calculated for (a) divalent and (b) trivalent dopants on the Fe and Si sites, respectively.

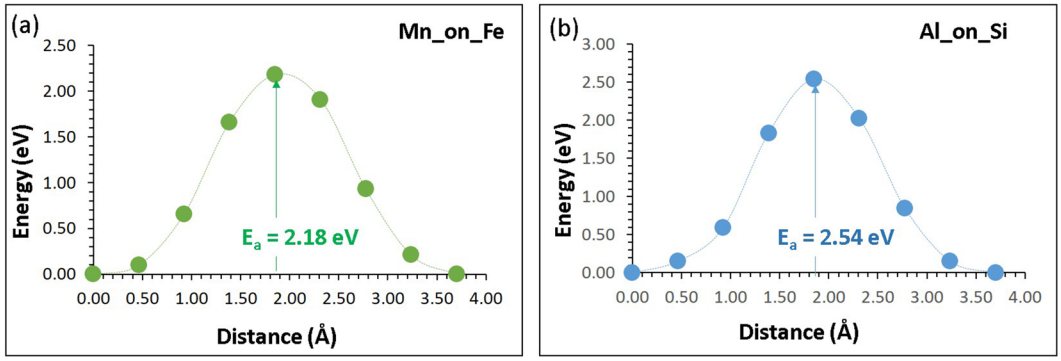

FIG. 6. Energy profile diagrams for the Ca local hops in the presence of (a) Mn^{2+} on the Fe site and (b) Al^{3+} on the Si site (refer to Fig. 3).

3. Tetravalent dopants

Finally, tetravalent dopants (M = Ge, Ti, Sn, Zr, and Ce) were considered on the Si site. Solution enthalpies are reported in Fig. 4(c). The following defect equation explains the mechanism involved in this process,

$$MO_2 + Si_{Si}^{X} \rightarrow M_{Si}^{X} + SiO_2. \quad (19)$$

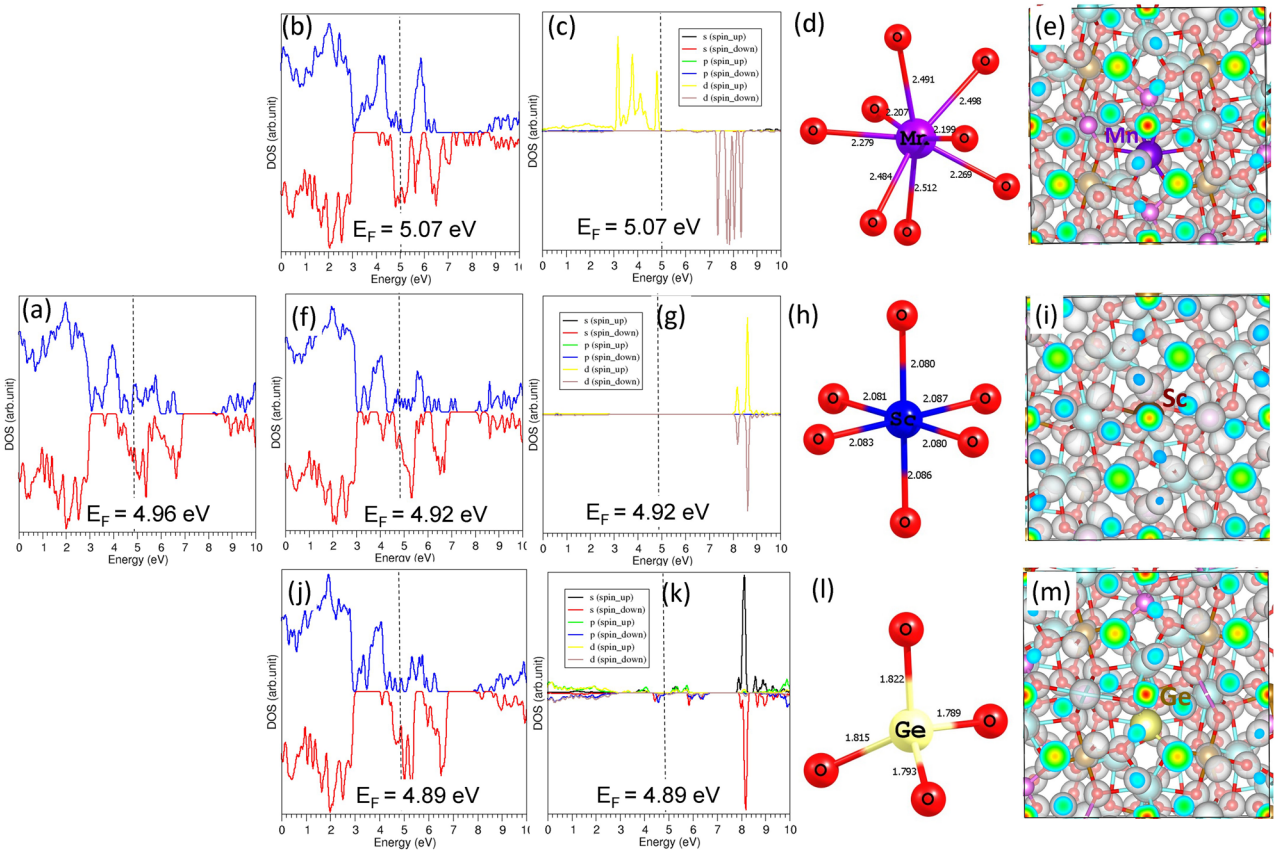

FIG. 7. (a) DOS plot of bulk $Ca_3Fe_2Si_3O_{12}$, (b) the DOS plot of Mn-doped $Ca_3Fe_2Si_3O_{12}$, (c) the atomic DOS plot of Mn, (d) the optimized MnO_8 unit with bond distance, (e) the constant charge density plot of Mn-doped $Ca_3Fe_2Si_3O_{12}$, (f) the DOS plot of Sc-doped $Ca_3Fe_2Si_3O_{12}$, (g) the atomic DOS plot of Sc, (h) the optimized ScO_6 unit with bond distance, (i) the constant charge density plot of Sc-doped $Ca_3Fe_2Si_3O_{12}$, (j) the DOS plot of Ge-doped $Ca_3Fe_2Si_3O_{12}$, (k) the atomic DOS plot of Ge, (l) the optimized GeO_4 unit with bond distance, and (m) the constant charge density plot of Ge-doped $Ca_3Fe_2Si_3O_{12}$.

The most favorable solution energy (0.43 eV) is calculated for Ge^{4+}. This is due to the ionic radius of Ge^{4+} (0.39 Å) being closer to that of Si^{4+} (0.26 Å). The solution enthalpy for Ti^{4+} is 3.86 eV, meaning that it is an unfavorable dopant. The second favorable dopant is Sn^{4+}, with a solution enthalpy of 2.10 eV. Solution enthalpy gradually increases with an increase in the ionic radius. The highest enthalpy of solution for Ce^{4+} (4.12 eV) suggests that doping would require external heat energy.

E. Ca-diffusion in the presence of dopants

Here, we calculate the activation energies for Ca-ion diffusion in the presence of Mn^{2+} on the Fe site and Al^{3+} on the Si site. Figure 6 shows the energy profile diagrams for the local Ca hops. There is a reduction (by 0.45 eV) in the activation energy for the doping of Mn^{2+} on the Fe site [refer to Fig. 6(a)]. In the case of doping of Al^{3+} on the Si site, activation energy is reduced only by 0.09 eV [refer to Fig. 6(b)]. In both cases, Ca–Ca distances have been slightly elongated compared to the distances present in the un-doped crystal structure. This perturbation in distances is due to the charge and ionic radius mismatch between Mn^{2+} and Fe^{3+} and Al^{3+} and Si^{4+}. The current simulation shows that doping of Mn^{2+} and Al^{3+} would simultaneously increase the concentration of Ca^{2+} ions in the lattice and reduce the activation energy of the Ca-ion migration.

F. Electronic structure of doped $Ca_3Fe_2Si_3O_{12}$

DFT simulations were used to examine the electronic structures of doped configurations. Here, we discuss the results of the most favorable dopants (Mn^{2+}, Ga^{3+}, Al^{3+}, and Ge^{4+}), as discussed in the previous sections.

The DOS plot calculated for bulk $Ca_3Fe_2Si_3O_{12}$ is shown in Fig. 6(a). Metallic behavior is observed for the ferromagnetic configuration of bulk $Ca_3Fe_2Si_3O_{12}$. Doping of Mn alters the electronic structure slightly, as shown in the DOS plot [refer to Fig. 7(b)]. Peaks arising from the 3*d* states of Mn appear near the Fermi level [refer to Fig. 7(c)]. Calculated Mn–O bond distances (2.20 Å–2.50 Å) [refer to Fig. 7(d)] are slightly shorter than the Ca–O (2.37 Å–2.54 Å) bond distances due to the ionic radius of Mn^{2+} being smaller than that of Ca^{2+}. The constant charge density plot of the Mn-doped configuration is shown in Fig. 7(e).

In the case of Sc, the Fermi level does not change significantly, and the doped configuration maintains its metallic behavior [refer to Fig. 7(f)]. The Fermi level does not have any contribution from Sc. States associated with Sc appear at ~8 eV in the conduction band [refer to Fig. 7(g)]. Sc–O bond distances are slightly longer (by ~0.04 Å) than the Fe–O bond distances. This is due to the ionic radius of Sc^{3+} being larger than that of Fe^{3+}, as discussed in Sec. III D 2.

Doping of Ge on the Si site has a little effect on the DOS structure [refer to Fig. 7(j)]. The doped configuration exhibits metallic behavior. Small peaks that belong to the 3*s* and 3*p* states of Ge appear just below the Fermi level [refer to Fig. 7(k)]. The Si–O bond distance in pristine $Ca_3Fe_2Si_3O_{12}$ is 1.66 Å. The Ge–O bond distances are longer than (by 0.15 Å) the Si–O bond distances. This is because of the ionic radius of Ge^{4+} (0.39 Å) being larger than that of Si^{4+} (0.26 Å).

Doping of Al on the Si site shifts the Fermi energy level only by 0.02 eV [refer to Fig. 8(b)]. The doped configuration is metallic. Additional peaks arising from 3*s* and 3*p* states of Al appear near the Fermi level [refer to Fig. 8(c)]. The calculated Al–O bond distances (1.77 Å) are longer than the Si–O bond distances (1.66 Å). This is because of the ionic radius and charge density of Al^{3+} being larger and smaller, respectively, than that of Si^{4+}.

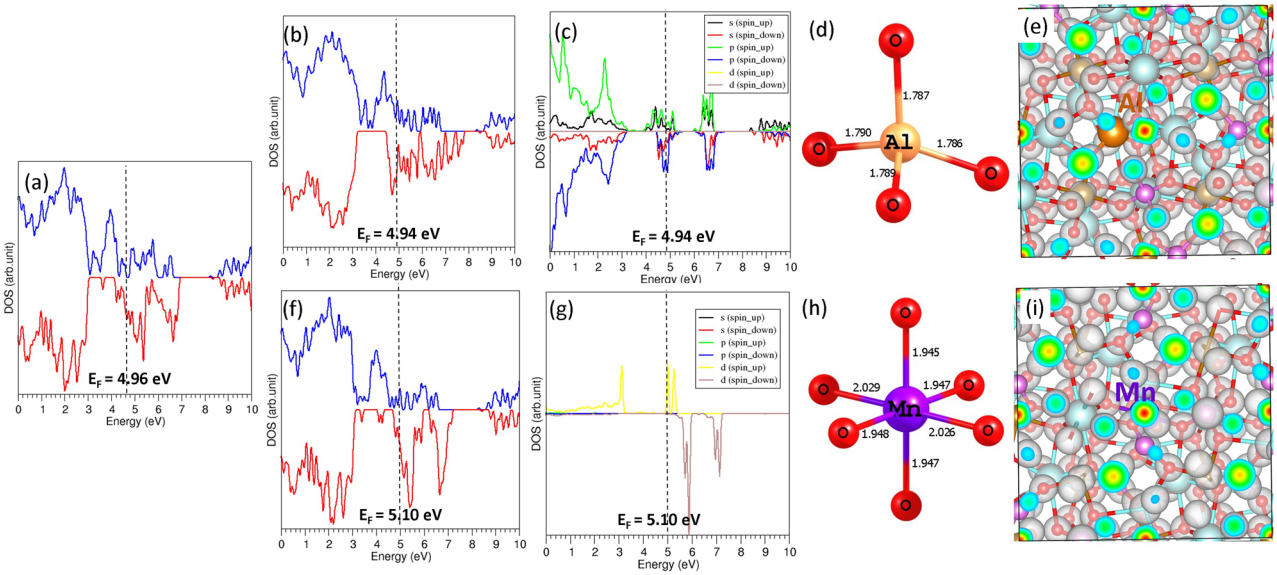

FIG. 8. (a) DOS plot of bulk $Ca_3Fe_2Si_3O_{12}$, (b) the DOS plot of Al-doped $Ca_3Fe_2Si_3O_{12}$, (c) the atomic DOS plot of Al, (d) the optimized AlO_4 unit with bond distance, (e) the constant charge density plot of Al-doped $Ca_3Fe_2Si_3O_{12}$, (f) the DOS plot of Mn-doped $Ca_3Fe_2Si_3O_{12}$, (g) the atomic DOS plot of Mn, (h) the optimized MnO_6 unit with bond distance, and (i) the constant charge density plot of Mn-doped $Ca_3Fe_2Si_3O_{12}$.

There is a slight shift in the Fermi energy level by 0.14 eV upon doping of Mn on the Fe site. Peaks associated with Mn appear near the Fermi level and in the valence band. Metallic behavior is still maintained. A very small perturbation is observed in the Mn–O bond distances compared to Fe–O bond distances. This is due to the small difference in the ionic radius and charge mismatch. The constant charge density plot of Mn doped on the Fe site in $Ca_3Fe_2Si_3O_{12}$ is shown in Fig. 8(h).

IV. CONCLUSIONS

Computational simulation was applied to analyze the behavior of the defects, diffusion pathways, and dopant properties in $Ca_3Fe_2Si_3O_{12}$. The Ca/Fe anti-site defect was predicted to be the most energetically favorable intrinsic defect process. The activation energy for three dimensional Ca vacancy migration in $Ca_3Fe_2Si_3O_{12}$ was calculated to be 2.63 eV, inferring low calcium mobility. Low solution energies were calculated for Mn^{2+}, Sc^{3+}, and Ge^{4+} on the Ca, Fe, and Si sites, respectively. Here, we show that Al^{3+} and Mn^{2+} are promising dopants on the Si and Fe sites, respectively, to introduce additional Ca in the form of Ca interstitials in $Ca_3Fe_2Si_3O_{12}$ for improving its capacity and Ca-ion diffusion. The difference in the electronic properties between un-doped and doped configurations was explained using electronic structures calculated using DFT.

SUPPLEMENTARY MATERIAL

See the supplementary material for the Buckingham potentials used in the classical simulation of the current study.

ACKNOWLEDGMENTS

Computational facilities and support were provided by the High Performance Computing Centre at Imperial College London.

This research was financially supported by the European Union's H2020 Programme under Grant Agreement No. 824072–HARVESTORE.

The authors declare that there is no competing financial interest.

DATA AVAILABILITY

The data that support the findings of this study are available from the corresponding author upon reasonable request.

REFERENCES

[1] J. B. Goodenough and K.-S. Park, J. Am. Chem. Soc. **135**, 1167 (2013).
[2] N. Nitta, F. Wu, J. T. Lee, and G. Yushin, Mater. Today **18**, 252 (2015).
[3] E. E. Jay, M. J. D. Rushton, A. Chroneos, R. W. Grimes, and J. A. Kilner, Phys. Chem. Chem. Phys. **17**, 178 (2015).
[4] M. Li, J. Lu, Z. Chen, and K. Amine, Adv. Mater. **30**, 1800561 (2018).
[5] D. Monti, A. Ponrouch, R. B. Araujo, F. Barde, P. Johansson, and M. R. Palacín, Front. Chem. **7**, 79 (2019).
[6] R. J. Gummow, G. Vamvounis, M. B. Kannan, and Y. He, Adv. Mater. **30**, 1801702 (2018).
[7] Y. Zhang *et al.*, Chem. Eng. J. **392**, 123652 (2020).
[8] G. Liu, Q. Chi, Y. Zhang, Q. Chen, C. Zhang, K. Zhu, and D. Cao, Chem. Commun. **54**, 9474 (2018).
[9] A. L. Lipson, B. Pan, S. H. Lapidus, C. Liao, J. T. Vaughey, and B. J. Ingram, Chem. Mater. **27**, 8442 (2015).
[10] G. G. Amatucci *et al.*, J. Electrochem. Soc. **148**, A940 (2001).
[11] T. R. Juran and M. Smeu, Phys. Chem. Chem. Phys. **19**, 20684 (2017).
[12] M. E. Arroyo-de Dompablo, C. Krich, J. Nava-Avendaño, N. Biškup, M. R. Palacín, and F. Bardé, Chem. Mater. **28**, 6886 (2016).
[13] A. Torres, F. J. Luque, J. Tortajada, and M. E. Arroyo-de Dompablo, Sci. Rep. **9**, 9644 (2019).
[14] M. S. Islam, R. Dominko, C. Masquelier, C. Sirisopanaporn, A. R. Armstrong, and P. G. Bruce, J. Mater. Chem. **21**, 9811 (2011).
[15] J. M. Clark, C. Eames, M. Reynaud, G. Rousse, J.-N. Chotard, J.-M. Tarascon, and M. S. Islam, J. Mater. Chem. A **2**, 7446 (2014).
[16] S. M. Wood, C. Eames, E. Kendrick, and M. S. Islam, J. Phys. Chem. C **119**, 15935 (2015).
[17] G. A. Novak and G. V. Gibbs, Am. Mineral. **56**, 791 (1971).
[18] N. Kuganathan and M. S. Islam, Chem. Mater. **21**, 5196 (2009).
[19] C. A. J. Fisher, N. Kuganathan, and M. S. Islam, J. Mater. Chem. A **1**, 4207 (2013).
[20] R. Kaushalya, P. Iyngaran, N. Kuganathan, and A. Chroneos, Energies **12**, 3094 (2019).
[21] J. Heath, H. Chen, and M. S. Islam, J. Mater. Chem. A **5**, 13161 (2017).
[22] M. Cherry, M. S. Islam, and C. R. A. Catlow, J. Solid State Chem. **118**, 125 (1995).
[23] J. D. Gale and A. L. Rohl, Mol. Simul. **29**, 291 (2003).
[24] J. D. Gale, J. Chem. Soc., Faraday Trans. **93**, 629 (1997).
[25] N. F. Mott and M. J. Littleton, Trans. Faraday Soc. **34**, 485 (1938).
[26] P. Varotsos, Phys. Rev. B **76**, 092106 (2007).
[27] P. Varotsos, J. Appl. Phys. **101**, 123503 (2007).
[28] A. Chroneos and R. V. Vovk, Solid State Ionics **274**, 1 (2015).
[29] M. W. D. Cooper, R. W. Grimes, M. E. Fitzpatrick, and A. Chroneos, Solid State Ionics **282**, 26 (2015).
[30] G. Kresse and J. Furthmüller, Phys. Rev. B **54**, 11169 (1996).
[31] J. P. Perdew, K. Burke, and M. Ernzerhof, Phys. Rev. Lett. **77**, 3865 (1996).
[32] H. J. Monkhorst and J. D. Pack, Phys. Rev. B **13**, 5188 (1976).
[33] W. H. Press, S. A. Teukolsky, W. T. Vetterling, and B. P. Flannery, *Numerical Recipes in C: The Art of Scientific Computing*, 2nd ed. (Cambridge University Press, 1992).
[34] S. Grimme, J. Antony, S. Ehrlich, and H. Krieg, J. Chem. Phys. **132**, 154104 (2010).
[35] N. Kuganathan, A. Kordatos, M. E. Fitzpatrick, R. V. Vovk, and A. Chroneos, Solid State Ionics **327**, 93 (2018).
[36] A. R. Armstrong, N. Kuganathan, M. S. Islam, and P. G. Bruce, J. Am. Chem. Soc. **133**, 13031 (2011).
[37] N. Kuganathan and A. Chroneos, Sci. Rep. **9**, 333 (2019).
[38] M. Kempaiah Devaraju, Q. Duc Truong, H. Hyodo, Y. Sasaki, and I. Honma, Sci. Rep. **5**, 11041 (2015).
[39] A. Nytén, A. Abouimrane, M. Armand, T. Gustafsson, and J. O. Thomas, Electrochem. Commun. **7**, 156 (2005).
[40] V. V. Politaev, A. A. Petrenko, V. B. Nalbandyan, B. S. Medvedev, and E. S. Shvetsova, J. Solid State Chem. **180**, 1045 (2007).
[41] F. A. Kröger and H. J. Vink, in *Solid State Physics*, edited by F. Seitz and D. Turnbull (Academic Press, 1956), Vol. 3, p. 307.
[42] N. Kuganathan, P. Iyngaran, and A. Chroneos, Sci. Rep. **8**, 5832 (2018).
[43] A. Kordatos, N. Kuganathan, N. Kelaidis, P. Iyngaran, and A. Chroneos, Sci. Rep. **8**, 6754 (2018).
[44] C. A. J. Fisher, V. M. Hart Prieto, and M. S. Islam, Chem. Mater. **20**, 5907 (2008).
[45] S.-i. Nishimura, G. Kobayashi, K. Ohoyama, R. Kanno, M. Yashima, and A. Yamada, Nat. Mater. **7**, 707 (2008).
[46] T. V. S. L. Satyavani, B. Ramya Kiran, V. Rajesh Kumar, A. Srinivas Kumar, and S. V. Naidu, Eng. Sci. Technol. **19**, 40 (2016).
[47] N. Kuganathan and A. Chroneos, Energies **13**, 1285 (2020).
[48] P. Arunkumar, W. J. Jeong, S. Won, and W. B. Im, J. Power Sources **324**, 428 (2016).